

# HOT GASEOUS ATMOSPHERES IN GALAXY GROUPS AND CLUSTERS ARE BOTH HEATED AND COOLED BY X-RAY CAVITIES

FABRIZIO BRIGHENTI<sup>1,2</sup>, WILLIAM G. MATHEWS<sup>1</sup>, PASQUALE TEMI<sup>3</sup>

*Draft version February 2, 2015*

## ABSTRACT

Expanding X-ray cavities observed in hot gas atmospheres of many galaxy groups and clusters generate shock waves and turbulence that are primary heating mechanisms required to avoid uninhibited radiatively cooling flows which are not observed. However, we show here that the evolution of buoyant cavities also stimulates radiative cooling of observable masses of low-temperature gas. During their early evolution, radiative cooling occurs in the wakes of buoyant cavities in two locations: in thin radial filaments parallel to the buoyant velocity and more broadly in gas compressed beneath rising cavities. Radiation from these sustained compressions removes entropy from the hot gas. Gas experiencing the largest entropy loss cools first, followed by gas with progressively less entropy loss. Most cooling occurs at late times,  $\sim 10^8 - 10^9$  yrs, long after the X-ray cavities have disrupted and are impossible to detect. During these late times, slightly denser low entropy gas sinks slowly toward the centers of the hot atmospheres where it cools intermittently, forming clouds near the cluster center. Single cavities of energy  $10^{57} - 10^{58}$  ergs in the atmosphere of the NGC 5044 group create  $10^8 - 10^9 M_{\odot}$  of cooled gas, exceeding the mass of extended molecular gas currently observed in that group. The cooled gas clouds we compute share many attributes with molecular clouds recently observed in NGC 5044 with ALMA: self-gravitationally unbound, dust-free, quasi-randomly distributed within a few kpc around the group center.

## 1. INTRODUCTION

Cavities are visible in the hot atmospheres of about 30 percent of all X-ray bright galaxy groups and clusters, but this percentage rises sharply with decreasing radiative cooling time of the central gas (e.g. Panagoulia et al. 2014). It is generally thought that powerful cavity-producing jets are released by cluster-centered massive black holes soon after accreting a small amount of cooled cluster gas. By feeding energy back into the cluster gas, the black hole increases the entropy and cooling time of nearby (and distant) gas in the surrounding atmosphere, maintaining the accretion rate at an acceptably low level. Weak shock waves produced by jets and their expanding cavities propagate far into the hot atmosphere, dissipating their energy. Cavity buoyant motion generates subsonic turbulence which can also contribute to gas heating (Dennis & Chandran 2005). By measuring the PV work done on the cluster gas by the cavities, it is possible to determine a lower limit to the rate that the atmospheres gain energy, although the total power delivered may greatly exceed this lower limit (Mathews & Guo 2011).

While cavities are likely to be a primary heating mechanism required to offset radiative cooling in hot group/cluster atmospheres, our goal here is to demonstrate that the mere presence of cavities, regardless of the mechanism that forms them, also stimulates profound inhomogeneous cooling in the hot gas over long times (see

also Brighenti & Mathews 2002). We do not consider the entire AGN feedback process in this paper in which cooling flows are suppressed by recurrent bubble heating (see, for example Brighenti & Mathews 2002, 2003, Dalla Vecchia et al., 2004, Mathews 2009), but instead limit our computations to study the influence of single X-ray cavities on the surrounding gas. Much is known from recent computational studies about the dynamics of cavity formation and their subsequent evolution (e.g. Bruggen 2003; Jones & De Young 2005; Reynolds et al. 2005; Gardini 2007; Ruszkowski et al. 2007; Revaz, Combes & Salome 2008; Mathews & Brighenti 2008; Bruggen, Scannapieco & Heinz, 2009; Dong & Stone 2009; O'Neill, De Young & Jones 2009; Guo & Mathews 2011), but few of these studies examine localized radiative cooling stimulated by cavity evolution. It is widely known that buoyantly rising cavities cause outflowing streams or filaments of (low entropy) cluster gas to rise up behind them. Revaz, Combes & Salome (2008) demonstrate that some of this rising gas cools radiatively, possibly explaining radial filaments observed in H $\alpha$  (e.g. Conselice et al. 2001) as well as kinematically related columns of colder molecular gas (Salome & Combes 2004; Ho et al. 2009; Lim et al. 2012). Recent investigations suggest that spatially extended cooling can occur in galaxy clusters where the ratio of cooling time to dynamical time is  $t_{cool}/t_{dyn} \lesssim 10$ , provided the ICM is endowed with non-linear density perturbations (McCourt et al. 2012, Sharma et al. 2012, Gaspari et al. 2012). Our main objective is to show that the buoyant motion of cavities stimulates intermittent cooling in the hot virialized gas in galaxies, groups and clusters. Cavity-cooled gas is distributed over kpc scales and lasts  $10^8 - 10^9$  yrs. No *ad hoc* distributed heating or artificial turbulent velocity field are necessary to form cooling perturbations. Valentini & Brighenti (2015) explore AGN induced cooling process in massive and in-

<sup>1</sup> University of California Observatories/Lick Observatory, Department of Astronomy and Astrophysics, University of California, Santa Cruz, CA 95064 (mathews@ucolick.org).

<sup>2</sup> Dipartimento di Astronomia, Università di Bologna, via Ranzani 1, Bologna 40127, Italy (fabrizio.brighenti@unibo.it).

<sup>3</sup> Astrophysics Branch, NASA/Ames Research Center, MS 245-6, Moffett Field, CA 94035 (pasquale.temi@nasa.gov).

intermediate elliptical galaxies and show that it occurs for  $t_{cool}/t_{dyn} \lesssim 70$ .

Molecular CO(2-1) emission was recently discovered in the bright group-centered elliptical galaxy NGC 5044 with single-dish IRAM sub-millimeter observations (see David et al. 2014). The molecular gas has a total mass  $\sim 10^8 M_{\odot}$ . This curious and unexpected result was confirmed with ALMA observations by David et al. (2014) who determined that much of the CO(2-1) emission was due to 24 spatially distinct clouds or cloud-aggregations in the hot atmosphere within 2 kpc of the group center. NGC 5044 has a vigorously active central black hole that feeds accretion energy back into its hot atmosphere – this is not the astronomical environment traditionally thought to create or harbor molecular clouds. The CO clouds are spatially unrelated to extended, optically absorbing dust patches seen in NGC 5044. They appear to be dust-free and self-gravitationally unbound. This suggests that the clouds may be currently cooling directly from the hot group atmosphere in NGC 5044 in a manner similar to the inhomogeneous cooling regions we calculate here.

In the following we review some of the numerical difficulties encountered when computing radiative cooling in Eulerian hydrodynamic flows. Fortunately, these difficulties can be largely overcome with a subgrid cooling scheme and we apply this scheme to cavity dynamics in group/cluster atmospheres having multi-keV temperatures. We find that radiative cooling is enhanced not only in radial filaments beneath buoyant cavities but also across the base of the cavities. Even more remarkable, we find that additional significant off-center radiative cooling may persist long after the observable lifetimes of the cavities responsible.

## 2. COMPUTATIONAL STRATEGY

We consider solutions of the standard hydrodynamic equations:

$$\frac{\partial \rho}{\partial t} + \nabla \cdot \rho \mathbf{u} = 0 \quad (1)$$

$$\rho \left( \frac{\partial \mathbf{u}}{\partial t} + (\mathbf{u} \cdot \nabla) \mathbf{u} \right) = -\nabla P + \rho \mathbf{g} \quad (2)$$

and

$$\frac{\partial e}{\partial t} + \nabla \cdot \mathbf{u} e = -P(\nabla \cdot \mathbf{u}) - \left( \frac{\rho}{m_p} \right)^2 \Lambda \quad (3)$$

where  $e = (\gamma - 1)P$  is the thermal energy density. The coefficient  $\Lambda(T)$  in the term for optically thin radiative cooling is that of Sutherland & Dopita (1993), evaluated with solar abundances.

We solve these equations in 2D cylindrical coordinates using a staggered ZEUS code (Stone & Norman 1992). 2D hydro allows us to consider very high numerical resolution, with computational zones as small as 5 pc. Also with 2D we can compare a large number of high resolution calculations with different parameters. In all calculations discussed below the grid is uniform throughout the region of interest, usually  $z \times R = 20 \times 8$  kpc or  $40 \times 16$  in more extended computations. Beyond the uniform region, 100 zones of progressively increasing size extend the grid to  $\sim 700$  kpc in both directions. We adopt standard reflecting boundary conditions at the  $R = 0$  and  $z = 0$

edges and outflow boundary conditions at the outer borders.

Computational difficulties arise when localized, low entropy, pressure equilibrium perturbations are imposed in gravitationally bound, radiating atmospheres like those in galaxy groups and clusters. Such perturbations, with lower gas temperature and higher density, are initially in pressure balance with the ambient hot cluster gas. But this equilibrium is immediately broken: gravity attracts the denser perturbation toward the cluster center where the higher ambient pressure enhances radiative losses, further amplifying the density perturbation. Idealized coherent perturbations with small or modest amplitude would undergo radial oscillations at the Brunt-Väisälä period, having oscillation-averaged cooling times that are nearly the same as that of the local cluster gas (e.g. Malagoli, Rosner & Bodo 1987; Loewenstein 1989). However, in reality and in numerical computations, perturbations are never perfectly coherent. In fixed grid Eulerian computations, which we consider here, the perturbation moves across the computational grid. In general, after each time step, as the perturbation moves across the computational grid, every grid zone has a temperature and density that is a mass average of the remaining original gas in that zone and gas that has flowed into it. As a result of this numerical mixing, the computed rate that gas cools in the perturbation can either underestimate or overestimate the radiative cooling that actually occurs.

The mass of gas that cools below some specified low temperature is computationally underestimated if the internal energy in the grid-crossing perturbation increases by numerical mixing with cluster gas faster than it can cool by its own radiative losses. As a result of numerical mixing, the amplitude of a moving entropy perturbation can decrease unrealistically fast. Conversely, the computed cooling rate can exceed the true cooling rate if the density contrast in a perturbed zone becomes sufficiently large relative to nearby cluster gas. Perturbations that successfully cool on the computational grid often develop zone to zone density and temperature variations that are inappropriately large for the linearized hydrodynamic difference equations (see Koyama & Inutsuka 2004). When only a small fraction of the mass in a dense cooled or cooling perturbation mixes with much hotter (and therefore less dense) gas in an adjacent zone, the numerically averaged temperature is also very low, causing the hot gas in the adjacent zone to cool much too rapidly. This spurious overcooling by numerical mixing is enhanced by the non-linear dependence of radiative cooling on the gas density and temperature. Computational experiments show that when the entropy in a single initial grid zone in a hot atmosphere is lowered beyond a certain threshold, its motion across the grid stimulates a total mass of cooled gas that can exceed its initial mass by orders of magnitude. As these overdense zones acquire a terminal infall velocity relative to the cluster gas, pressure gradients in nearby, hot gas drive localized radiating inflows toward the cooling and infalling zone, greatly increasing its cooling rate. Owing to non-linear cooling, the number of grid zones that cool usually does not increase; instead the cooled mass increasingly resides in only a very few zones. Based on our experience, non-linear overcooling zones with ultralow temperatures cannot be avoided simply by resorting to smaller computational grids.

As they fall across the grid moving into much hotter ambient gas, small regions of dense, cooled gas can trigger large unintended overcooling due to unphysical numerical mixing with the hotter gas. Conversely, in very slowly cooling, low amplitude, nearly adiabatic perturbations some degree of undercooling can be expected. Physical truth lies between these two extremes. In view of these difficulties, we have devised an appropriate sub-grid scheme to compute radiatively cooling gas more accurately.

### 2.0.1. Cooling Dropout

Numerical inaccuracies resulting in overcooling can be largely avoided by removing strongly cooling gas before it stimulates unphysical numerical cooling by advecting across the grid. To accomplish this, we employ a sub-grid mass dropout procedure similar to that described by Brighenti & Mathews (2002). Our sub-grid scheme is similar to early computations of cooling flows in which gas mass lost by star formation was represented with a sink term in the continuity equation  $-q\rho/t_{cool}$  with constant  $q$  (e.g. Fabian, Nulsen, & Canizares 1984; White & Sarazin 1987; further references in Mathews & Brighenti 2003). Assuming  $\Lambda \propto T^{-0.7}$  for  $10^6 \lesssim T \lesssim 10^7$  K, the sink term removes gas mass at a rate  $\rho/t_{cool} \propto \rho^2/T^{1.7}$ . We adopt here a modified temperature-dependent mass dropout coefficient  $q(T)$  that increases the sensitivity to cooling gas. The following mass dropout term is added to the right hand side of the continuity equation (Eqn. 1):

$$\left(\frac{\partial \rho}{\partial t}\right)_{do} = -q(T)\frac{\rho}{t_{cool}} \quad (4)$$

(Brighenti & Mathews 2002).

Since mass removal also results in a loss of thermal energy, a corresponding dropout term is also needed in the thermal energy equation (Eqn. 3):

$$\left(\frac{\partial e}{\partial t}\right)_{do} = -q(T)\frac{e}{t_{cool}} \quad (5)$$

For the dimensionless coefficient  $q(T)$  we adopt a function that increases rapidly with decreasing temperature,

$$q(T) = q_0 \exp[-(T/T_c)^2], \quad (6)$$

so the dropout term is negligible for  $T \gtrsim T_c$ . Accurate mass removal also requires the time step  $\Delta t$  be sufficiently small, allowing the temperature to decline slowly over many time steps even in the most rapidly cooling zones. Since the exponential term in  $q(T)$  dominates, the precise value of  $q_0$  hardly matters, and  $q_0 = 2$  is chosen to match our previous calculations. The threshold temperature  $T_c$ , below which mass dropout is strongly enhanced, must be small enough to allow accurate cooling down to temperature  $\sim T_c$  without significant mass dropout. Empirical computations with varying grid resolution and  $T_c$  converge to the same total mass of cooled gas provided  $T_c \lesssim 5 \times 10^5$  K. We note that the sink terms for dropout are proportional to  $t_{cool}^{-1} \propto \Lambda$  so that no-dropout occurs in adiabatic flow  $\Lambda = 0$ . In addition, high-resolution (small grid zones) provides more accuracy in defining the spatial extent of strong cooling.

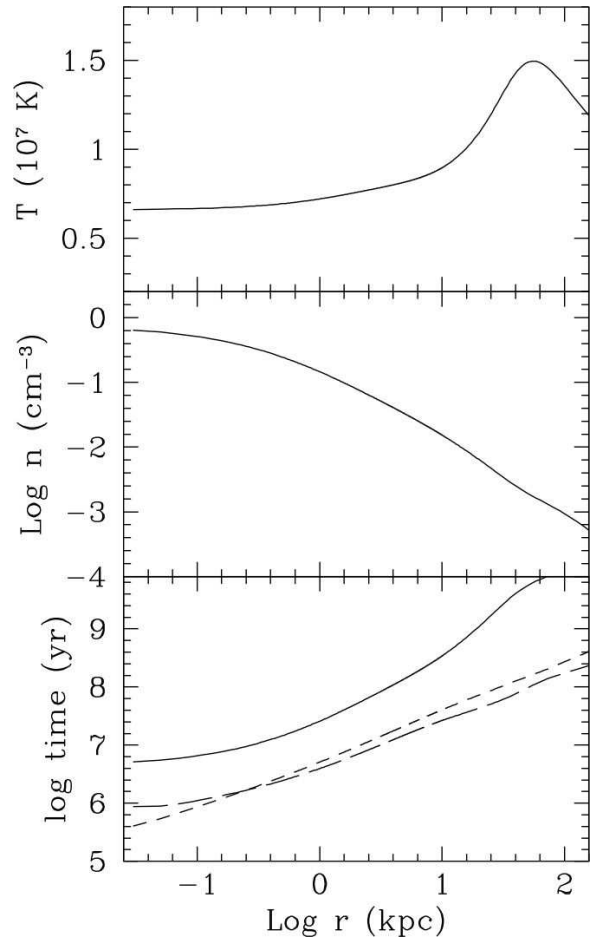


FIG. 1.— Hot gaseous atmosphere in the NGC 5044 group. *Upper panel:* gas temperature; *Center panel:* gas density; *Bottom panel:* time scales of interest: local cooling time (solid); local freefall time (short dashed line) and the Brunt-Väisälä time (long dashed line).

### 3. COOLING ASSOCIATED WITH CAVITY FORMATION

We now describe how the evolution of X-ray cavities stimulates significant off-center cooling of the hot gaseous atmospheres in galaxy groups and clusters. For this purpose we adopt the well-studied atmosphere in the NGC 5044 galaxy group at distance 31.2 Mpc (Tonry et al. 2001), although our results apply in general to any central galaxy in groups or clusters. The atmosphere of this luminous group contains extended multifrequency emission believed to result from AGN feedback events: filamentary optical line emission from warm ( $T \sim 10^4$  K) gas is observed out to  $\sim 10$  kpc (e.g. David et al. 2011); extended diffuse [CII] $\lambda 158\mu\text{m}$  emission (Werner et al. 2014); CO molecular emission within  $\sim 4$  kpc, much of which is contained in about two dozen small clouds (David et al. 2014), and  $70\mu\text{m}$  dust emission out to 7 – 10kpc where the sputtering time is only  $\sim 10^7$  yrs (Temi, Brighenti & Mathews 2007a,b). This dust has probably been transported outward from the core by AGN events (Mathews et al. 2013). The central AGN in NGC 5044 is visible as an X-ray point source.

The upper panel in Figure 1 shows our approximate fit to the temperature profiles from X-ray observations of NGC 5044 (David et al. 1994; Buote et al. 2003,2004; David et al. 2009) and the density (central panel) is determined from X-ray observations by assuming hydro-

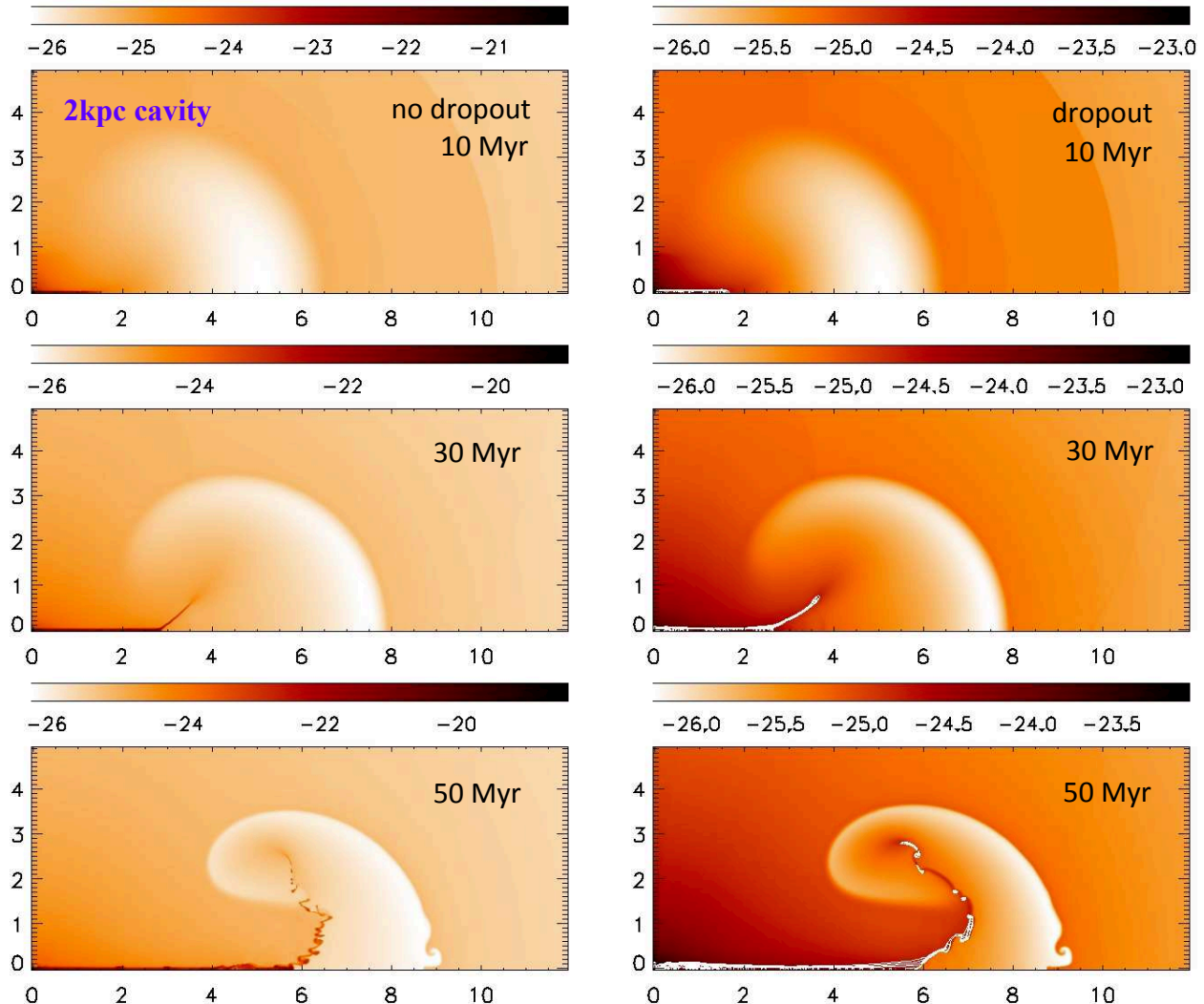


FIG. 2.— Gas density maps at various times for the 2 kpc cavity calculated without dropout (left panels) and with dropout (right panels). In the left panel, dark regions represents cooled gas at  $T = 10^4$  K. In the right panels, white grid zones indicate locations where the gas is currently dropping out of the flow (cooling to temperatures below  $T_c = 5 \times 10^5$  K). Axes in each panel in this and subsequent figures are labeled with  $z$  (horizontal) and  $R$  (vertical) coordinates in kpc.

static equilibrium. The adopted gravitational potential is the combination of a dark matter NFW halo (Navarro et al. 1996) (mass  $M_{\text{dm}} = 4 \times 10^{13} M_{\odot}$  and concentration  $c = 8.8$ ) and a de Vaucouleurs galaxy of mass  $M_* = 3.4 \times 10^{11} M_{\odot}$  and effective radius  $r_e = 10$  kpc. The bottom panel of Figure 1 shows several time scales of interest: the cooling time at constant pressure  $t_{\text{cool}} = 5m_p kT / 2\mu\rho\Lambda$ , the local freefall time  $t_{\text{ff}} \approx (|g|/2r)^{-1/2}$  and the Brunt-Väisälä time  $t_{\text{bv}} \approx [|g(d \ln \rho / dr)|]^{-1/2}$ . Hydrostatic equilibrium is assumed to hold in the initial spherical hot atmosphere,  $g = (1/\rho)dP/dr$ , where  $r$  is the radial coordinate.

All hydrodynamic calculations begin with a static spherical atmosphere having density and temperature profiles as in Figure 1. Immediately as the calculation begins, a cooling flow develops in the hot atmosphere and a cavity is created by heating gas in a small spherical region along the  $z$ -axis, generating an expanding cavity that drives a modest shock wave into the ambient gas. The heating continues for  $t_{\text{heat}} = 1$  Myr and provides a total internal energy  $E = 1.17 \times 10^{57}$  ergs to the atmo-

sphere, corresponding to a power of  $3.7 \times 10^{43}$  erg  $\text{s}^{-1}$ . This short cavity formation time is consistent with the absence of observable jets in most galaxy group cavities. In reality cavities are thought to be inflated by relativistic and/or ultra-hot gas transported from the central AGN by jets. Nevertheless, our conclusions about cooling during cavity evolution are quite general and are quite independent of the particular means of cavity inflation. In the discussion that follows cavities are defined by their fixed heating points in the NGC 5044 atmosphere, e.g. “2 kpc” or “5 kpc” cavities.

### 3.1. Evolution of the 2 kpc and 5 kpc cavities

Figures 2 and 3 show the gas density evolution of 2 kpc and 5 kpc cavities at selected times. Although the total thermal energy that formed both cavities is the same, their maximum transverse cavity radius increases from 3.4 to 4 kpc as the heating point moves from 2 to lower density gas at 5 kpc from the cluster center. Solutions with and without mass dropout are shown respectively in right and left panels of Figures 2 and 3. If there is no mass dropout ( $q(T) = 0$ ), gas cools to  $T = 10^4$  K then

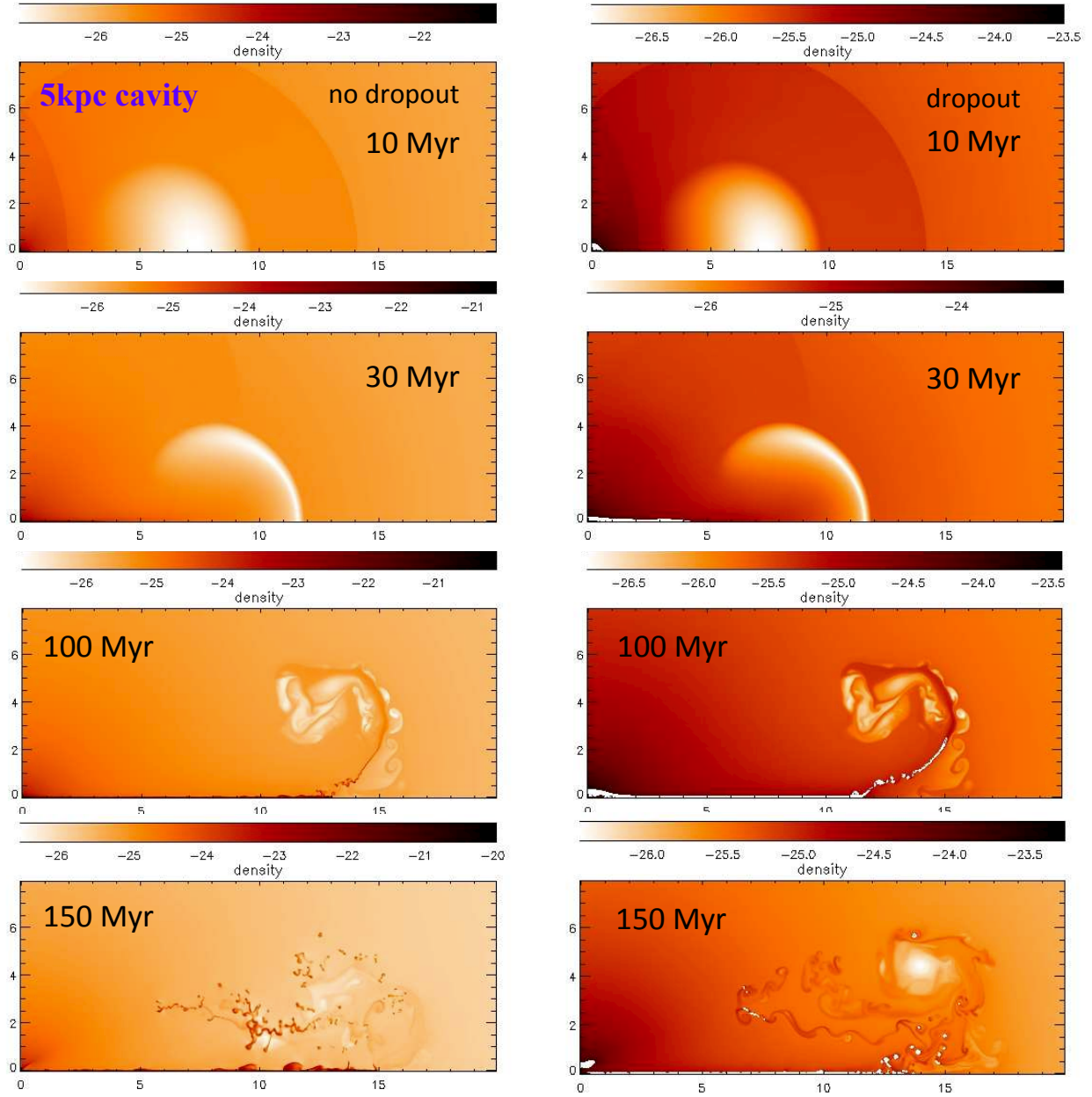


FIG. 3.— Same as Figure 2, but for the 5 kpc cavity.

remains on the grid, supposedly ionized by UV from old asymptotic branch giant stars, i.e.  $\Lambda(T) = 0$  for  $T < 10^4$  K. This type of arrested cooling endstate is plausible since as the gas cools, small magnetic fields in the initial gas increasing as  $B \propto \rho^{2/3}$  can ultimately provide enough magnetic pressure to balance the pressure of local hot gas (Fabian et al. 2008). Observations of the density-sensitive [SII] $\lambda 6716/6731$  flux ratio in extended warm ( $T \sim 10^4$  K) gas around M87 (Werner et al. 2013) indicate that the density increase in cooling gas may be magnetically arrested. When mass dropout at low temperatures is present and  $T_c = 5 \times 10^5$  K, as in the right hand panels in Figures 2 and 3, we show with white contours grid zones in which gas is currently dropping out. In dropout solutions cooled gas is removed from the grid and its subsequent dynamical motion is not followed. All cavity evolutions in Figures 2 and 3 were made at high spatial

resolution with uniform grid zones of size  $\Delta z = \Delta R = 20$  pc, i.e. each square kpc in the Figures contain  $50 \times 50 = 2500$  zones.

While the general appearance of cavities with and without mass dropout in Figures 2 and 3 are nearly the same, a detailed analysis of the cooling rate and the total accumulated mass of cooled gas shown in Figure 4 reveals significant differences. Several cooling rates are plotted in the left panels in Figure 4, describing the total cooling rate of cluster gas in the absence of cavity formation (dotted lines) and total cooling with (dashed lines) or without (solid lines) the dropout terms. (The long-dashed lines plotted near the bottom in the left panels are cooling rates in the “cavity region” and will be discussed further below.)

The single cavities we consider do not provide enough distributed long-term energy to stop radiative cooling

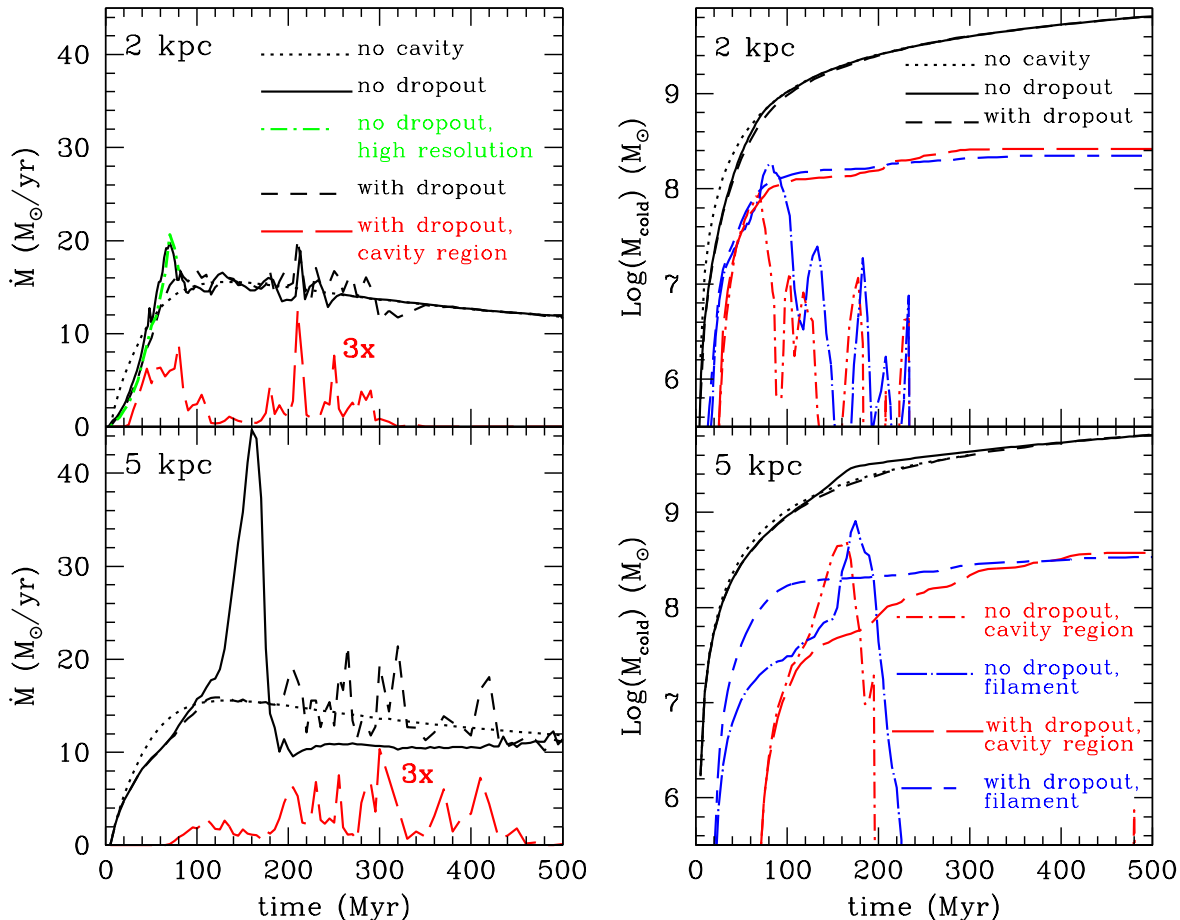


FIG. 4.— *Left panel:* Time variation of cooling rates  $\dot{M}$  for the 2 kpc cavity (upper panel) and 5 kpc cavity (lower panel). Dotted lines show the global cooling with no cavity. Solid lines represent models without dropout (i.e. gas cools to  $10^4$  K and stays on the grid). Dashed lines show models with dropout (in which the gas that cools to  $T \sim T_{\text{crit}} = 5 \cdot 10^5$  K is smoothly removed from the grid). Long dashed lines at the bottom of each panel plot three times the rate that gas drops out in the cavity region ( $z > 1$  kpc  $R > 0.3$  kpc). The green dash-dotted line (extending only to 80 Myr) shows a repeat of the no-dropout 2 kpc evolution at ultra-high grid resolution (5 pc,  $\Delta z = \Delta R = 5$  pc). *Right panel:* Time variation of the mass of cold gas (either cooled to  $T = 10^4$  K or dropped out). Dotted black lines near the top show the total mass of gas that cools at the center of the atmosphere when no cavity forms. Solid and dashed black lines near the top represent the total mass of cold gas without and with dropout respectively. For dropout flows: long dashed and long-short dashed lines are cumulative dropped out mass for the “cavity region” ( $z > 1$  kpc,  $R > 0.3$  kpc) and the “filament region” ( $z > 1$  kpc,  $R < 0.3$  kpc). For no-dropout flows: long-dash-dotted and short-dash-dotted lines are the total cold mass in the filament and cavity regions respectively. Blue lines denote cold gas in the “filament region” ( $z > 1$  kpc,  $R < 0.3$  kpc); red refers to cold gas in the “cavity region” ( $z > 1$  kpc,  $R > 0.3$  kpc).

near the center of the flow; to accomplish this would require more cavities with various locations and energies (Mathews 2009) which would mask and complicate the single cavity flows we describe here. Consequently, as seen in Figure 4, much of the cooling and cooled gas accumulates right at the center. During the initial 70-100 Myrs, as the cavities form and the atmosphere converts to a cooling flow, the cavities are seen to slightly reduce the total cooling rate. This reduction is apparently due to heating by the cavity shock and the large vortical flow generated around the buoyant cavity. As the outward moving cavity provides space to be filled in its wake, cluster gas flows down around the outer cavity boundary then circulates up from beneath the cavity, joined by low entropy gas closer to the cluster center that would have otherwise flowed to the center and cooled. The total cooling rate  $\dot{M}$  is reduced by this outward motion of low entropy gas in the cavity wake.

### 3.2. The cavity vortex flow

A snapshot of the velocity field at 50 Myrs in the buoyant 2 kpc cavity for the dropout solution is shown in the upper panel of Figure 5. The large vortex flows in a slanted fashion toward the symmetry  $z$ -axis and broadly up into the bottom of the cavity. This broader upflow provides a sustained compression in which much of the radiation and entropy losses occur during the early cavity evolution. Solutions without dropout are seen to undergo periods of intense cooling near 70 and 160 Myrs respectively for the 2 kpc and 5 kpc cavities (solid lines in Fig. 4, left panels). For both cavity models much cooling occurs in the “cavity region” away from the center or  $z$ -axis filament, as seen in the left panels of Figure 4. These peaks in the total cooling rate are due to numerical overcooling triggered by numerous cold clouds, clearly visible in the lowest left panel of Figure 3 for the 5 kpc

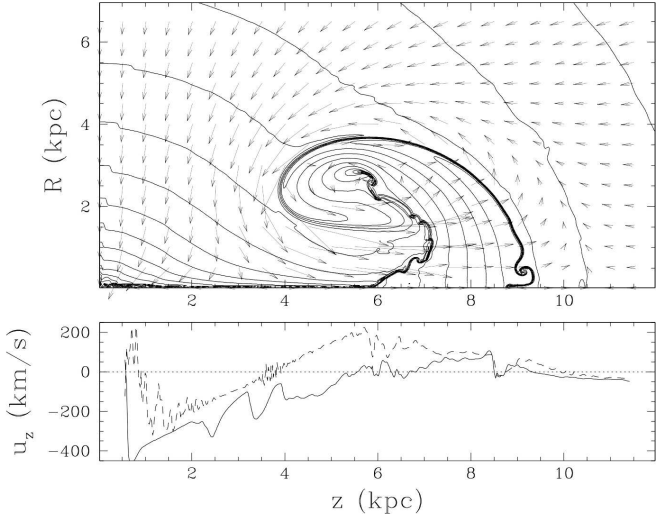


FIG. 5.— *Upper Panel:* Velocity field for dropout flow for 2 kpc cloud at 50 Myr. Arrows 1 kpc in length correspond to  $200 \text{ km s}^{-1}$ . Contours are for gas density. *Lower Panel:* Radial velocity along  $z$ -axis for 2 kpc cavity at time 50 Myr. Solid and dashed lines are for no-dropout and dropout flows respectively.

cavity model. However, these peak cooling rates are entirely absent when dropout is included (dashed lines in Fig. 4). The largest of these spurious cooling peaks in Figure 4, shown in the 5 kpc cavity at time 150 Myr (bottom left in Figure 3), occurs at a time when the cavity has largely disappeared and the off-axis no-dropout flow is dominated by many small and dense overcooling regions falling through the hot gas (and across the computational grid). So much gas overcools during the spurious 5 kpc cavity cooling peak in Figure 4 that the subsequent global cooling rate does not recover until about time 500 Myrs.

The radial velocity  $u_z(z)$  along the  $z$ -axis filament for the 2 kpc cloud at 50 Myr is plotted in the lower panel of Figure 5 for the dropout (dashed line) and no-dropout (solid line) solutions. The no-dropout solution is more irregular because small, dense clouds with temperature  $T = 10^4 \text{ K}$  continue to collide into the filament. These dense regions, usually only several grid zones in size, do not free fall in a perfectly radial direction toward the center of the flow, but are swept toward the filament along the  $z$ -axis by the hot gas vortex flowing beneath the cavity. The filament in the no-dropout solution, also at  $T = 10^4 \text{ K}$ , is denser and flows toward the center more rapidly than the filament in the dropout solution where hot gas is still cooling at temperatures  $T \gtrsim 10^5 \text{ K}$ . Note that the filament velocity  $u_z(z)$  passes through zero. The zero-velocity point typically moves out with time toward larger  $z$  (Mathews & Brighenti 2008).

### 3.3. Off-center cooling beneath cavities

The uppermost solid (no-dropout) and dashed (dropout) lines in the two right hand panels in Figure 4 show the total cumulative mass that either cooled or dropped out during the first 500 Myrs. The total cooled mass,  $6 \times 10^9 M_\odot$ , is nearly unaffected by dropout, initial location (2 or 5 kpc) of the cavity, or whether the cavity is present or not. Most of this global cooling occurs at

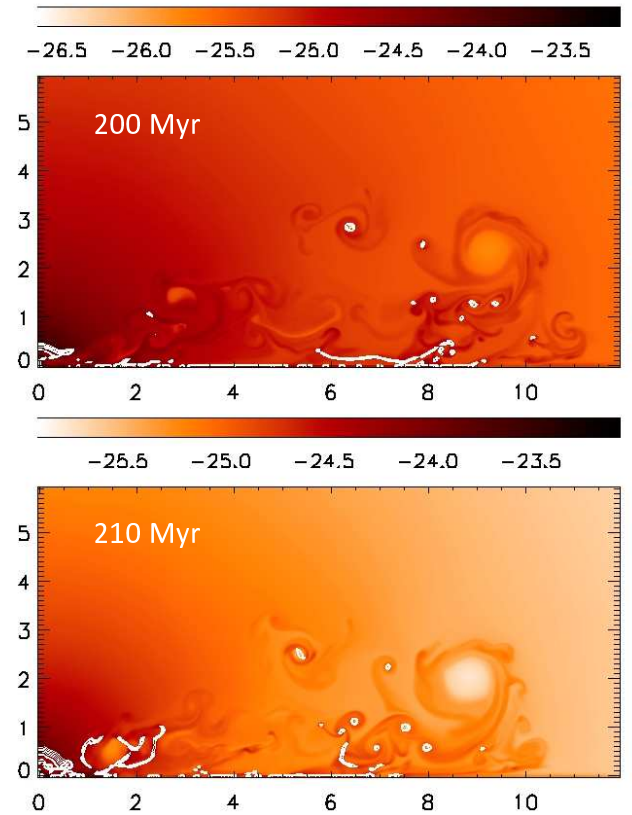


FIG. 6.— Density images for 2 kpc cavity dropout flow at 200 and 210 Myrs.

the origin<sup>4</sup> and could be reduced or eliminated by multi-cavity feedback events. Our interest here is the mass of non-central gas that cools along the  $z$ -axis filament and, especially, away from both the filament and the center.

To explore off-center cooling, we consider non-central cooling in two regions: the “filament region” along the  $z$ -axis ( $z > 1 \text{ kpc } R < 0.3 \text{ kpc}$ ) and the “cavity region” ( $z > 1 \text{ kpc } R > 0.3 \text{ kpc}$ ). Cooling in the radial filament and cavity regions are shown respectively with blue and red lines in Figure 4 or in terms of line types as explained in the figure caption.

The episodic cooling pattern during the no-dropout cavity evolution (right panel of Fig. 4) clearly indicates that some of the gas cools first in the cavity region then flows into the filament region, although much cooling occurs in gas flowing directly into the filament region. After gas enters the filament, it eventually flows with nearly freefall or terminal velocity into the core of the cluster-centered galaxy. This filament persists long after the cavity has become difficult to observe,  $t \gtrsim 70$  or 160 Myrs respectively for the 2 kpc and 5 kpc cavities. (The visibility of coherent cavities in Figures 2 and 3 may be degraded somewhat by residual numerical mixing.) Such radial filamentary features have been observed in warm gas emission in many groups and clusters. The perfectly focused, narrow width of the filaments we compute is due to the exactly static cluster gas prior to forming the axisymmetric cavity. In reality, the cluster gas is expected to have random subsonic motions due to feedback from previous generations of cavities, and this

<sup>4</sup> In the no-dropout case the cooled gas accumulates at the center, where it stays indefinitely.

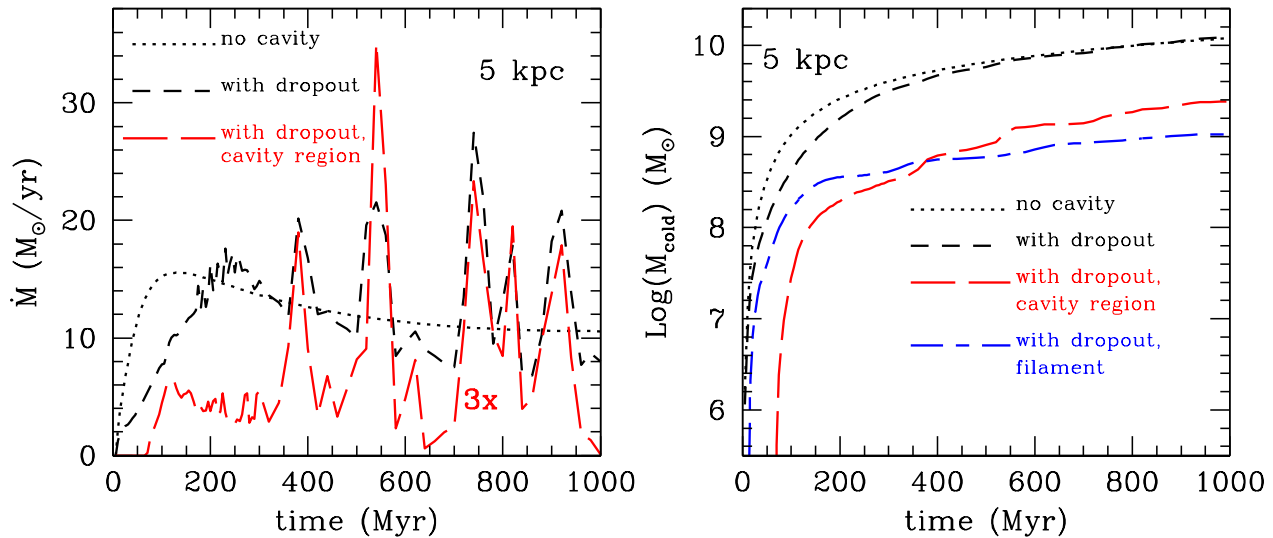


FIG. 7.— Cooling rate and total cumulative cooling for 5 kpc cavity with 10 times higher energy  $1.17 \times 10^{58}$  ergs. Line types and colors are the same as in Figure 4.

initial turbulence would deflect gas as it approaches the  $z$ -axis, broadening the filaments. In no-dropout calculations gas that cools episodically in the cavity region later flows into the filament region then into the origin, accounting for the time lag between cooling peaks in cavity and filament regions in Figure 4.

Red long dashed and blue long-short dashed lines in the right panels of Figure 4 show the total cumulative mass of gas that cooled or dropped out respectively in the cavity and filament regions. Slope changes (as in the red dashed line for the 2 kpc cavity at  $t \approx 210$  Myrs) indicate episodes of more intense cooling. Since we do not follow the dynamics of gas after it drops out, it is not possible to know where this gas is currently located, but as in the no-dropout case, most of it ultimately find its way to the origin or form stars.

The total mass of gas that cools off-center varies with time, but can be large. Dropout cavity calculations do not suffer from overcooling and the amount, time and location of gas that drops out is recorded during each dropout evolution. The cooling (or dropping out) rate  $\dot{M}_{cav}(t)$  of gas in the cavity region ( $z > 1$  kpc  $R > 0.3$  kpc) and the total mass of dropped out gas are plotted with dashed lines in the left panels of Figure 4, where for visibility  $\dot{M}_{cav}(t)$  is multiplied by 3. The 2 kpc cavity experienced sustained compression in the vortical upflow lasting about  $\delta t = 25$  Myr from  $\sim 40$  to  $\sim 65$  Myr. During this time, gas beneath the cavity is compressed sufficiently long to radiate away a substantial fraction of its entropy or to cool completely. Ongoing cooling of this gas is visible as white cooling regions dropping out in the density image for the 2 kpc cavity at time 50 Myrs in Figure 2. The total mass that cools during this cavity compression episode is the product of the dropout rate  $\dot{M}_{cav} \approx 2 M_{\odot} \text{ yr}^{-1}$  and the duration,  $\dot{M}_{cav} \delta t \approx 8 \times 10^7 M_{\odot}$ .

We note here that in real systems X-ray cavities are continuously created by the central AGN. While the effect of recurring cavities on the off-center cooling will be considered in a future work, we point out that pre-

liminary calculations validate the fundamental result described above. Intermittent cavities persistently generate regions of converging flow and non-linear density perturbations which originate spatially extended cold clouds (see also Brighenti & Mathews 2002).

### 3.4. Late time cooling

In addition to cooling during the initial cavity compression, Figure 4 indicates that the mass dropout rate in the cavity region  $\dot{M}_{cav}(t)$  continues to peak in an irregular fashion at much later times. In fact, the lower left panel of Figure 4 shows that the 5 kpc cavity cools considerably more mass at times  $t \gtrsim 200$  Myr after the cavity has largely disappeared than it does during the initial cavity compression at time  $t \sim 100$  Myr.

The 2 kpc cavity also exhibits a continued high rate of intermittent cooling until 300 Myrs. Consider for example the large late time cavity region mass dropout in the 2 kpc cavity event at  $\sim 210$  Myr. This dropout event at  $(R, z) \approx (0.5, 1.5)$  kpc lasts  $\delta t \approx 12.5$  Myr with mean  $\dot{M}_{cav} \approx 2 M_{\odot} \text{ yr}^{-1}$ , corresponding to a total cooled mass  $\sim 2.5 \times 10^7 M_{\odot}$ . Figure 6 shows the spatial distribution of this cooling gas at 200 Myrs just before this cooling event and at 210 Myrs when it peaked. The peak in the cavity region ( $z > 1$  kpc  $R > 0.3$  kpc) at 210 Myrs is apparently due to the irregular white features seen in Figure 6 at  $1.5 \lesssim z \lesssim 2.5$  kpc. Evidently, cluster gas that experienced a relatively small amount of entropy loss during compressions in the early cavity evolution eventually flows slowly inward and cools away from the cluster center. In pressure equilibrium gas with lower entropy has a higher density and sinks in the atmosphere. The complex cooling pattern that appears as curved filaments when viewed in the axisymmetric density slice in Figure 6 is actually toroidal. Nevertheless, it still has a filamentary appearance when viewed in projection. Many such curved, non-radial warm gas filaments have been observed in optical images in thermal line emission (e.g. Conselice et al. 2001; McDonald et al. 2012).

When observing the NGC 5044 group with the ALMA



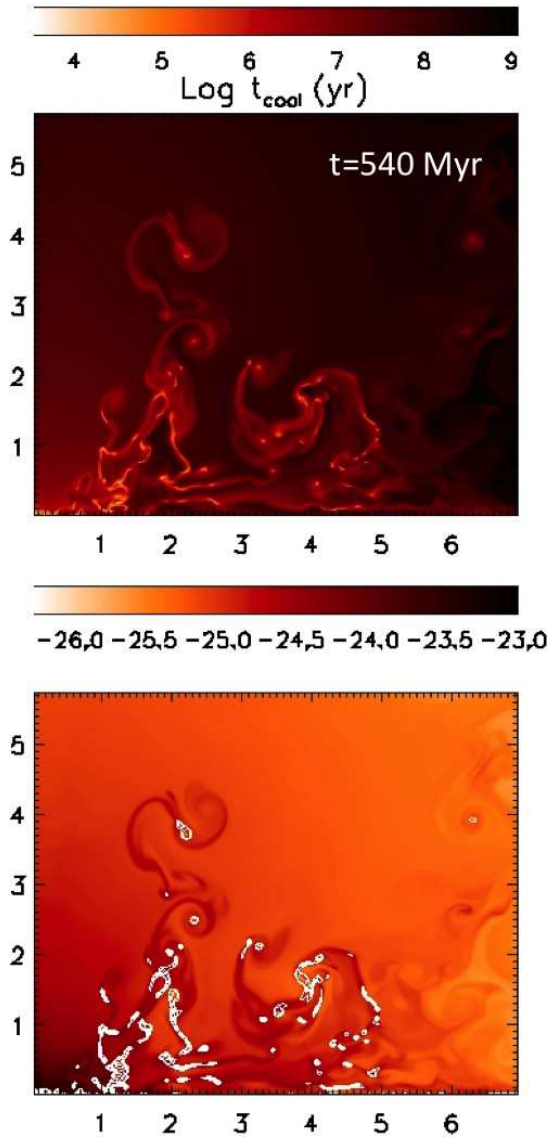


FIG. 8.— Cooling time  $t_{cool}$  (top) and gas density with currently dropping-out zones in white (bottom) near the center of the hot atmosphere for the high energy 5 kpc cavity at time  $t = 540$  Myr.

array, David et al. (2014) discovered about 2 dozen gravitationally unbound CO(2-1) molecular clouds having individual masses of  $10^5$  to  $10^7 M_\odot$  with a combined total mass of  $5 \times 10^7 M_\odot$ . Additional, more diffuse CO(2-1) emission within the central 1.6 kpc may have been resolved out by ALMA, as indicated by single dish IRAM 30m CO(2-1) observations that detect a total molecular mass in NGC 5044 of  $\sim 2 \times 10^8 M_\odot$ . These molecular masses are estimated by assuming that the Galactic CO to  $H_2$  conversion is appropriate. The array of cooling gas at  $(R, z) \approx (0.5, 1.5)$  kpc seen in the lower panel of Figure 6 has enough mass ( $\sim 2.5 \times 10^7 M_\odot$ ) to create 25 molecular clouds each of mass  $10^6 M_\odot$  within 2 kpc from the center, attributes similar to the clouds observed in NGC 5044 by David et al. (2014).

If molecules form in the late time cooling gas in our calculations, the resulting clouds would be unbound, dust-

free and rather randomly distributed in the central few kpcs. In these respects they resemble the CO clouds discovered in the NGC 5044 atmosphere by David et al. (2014).

Long dashed lines in the right panels of Figure 4 indicate that the total cold, dropped out mass in the cavity region due to the evolution of the 2 and 5 kpc cavities over 500 Myrs are  $2.6 \times 10^8 M_\odot$  and  $3.5 \times 10^8 M_\odot$  respectively. More gas cools in the cavity region when the same cavity energy is injected further out in the atmosphere, creating larger cavities. The total mass cooled over time by the 2 or 5 kpc cavities is comparable with the total molecular mass observed in NGC 5044 ( $\sim 2 \times 10^8 M_\odot$ ). Because of intermittent cooling, not all of the computed dropped out gas would be visible at any one time, so multiple or more energetic cavities would be required to continuously supply the CO(2-1) mass observed.

### 3.5. A more energetic cavity at 5 kpc

Figure 7 shows the cooling rate and total cooled gas identical to the 5 kpc cavity discussed earlier but now having 10 times more energy,  $1.17 \times 10^{58}$  ergs. Cooling in the cavity region continues to at least 1 Gyr when our calculation terminated. By 1 Gyr  $2.5 \times 10^9 M_\odot$  of gas cools in the cavity region at a remarkably high average rate  $\dot{M}_{cav} = 2.5 M_\odot \text{ yr}^{-1}$ . After 300 Myrs, when the cavity has largely disappeared, the cooling rate is dominated by 5 major events each lasting  $\sim 50$  Myrs when the cooling rate  $\dot{M}_{cav}$  exceeds  $4 M_\odot \text{ yr}^{-1}$ . During the largest cooling event at time 540 Myrs lasting  $\delta t \approx 40$  Myr, a total of  $2 \times 10^8 M_\odot$  cools in the cavity region. As seen in Figure 8, most of this gas cools within 5 kpc of the center, typical of late time cooling. The fate of the gas that cools in this dropout calculation is unclear, but it may remain as warm or molecular gas for a long time after it cools by dropout so it may be possible to observe this cold gas long after each peak in the cooling rate in Figure 7.

### 3.6. Velocity distribution of the cold gas

It is interesting to investigate the velocity distribution of the cold gas generated by the "cavity-cooling" process. In the following we focus on the cold clouds in the cavity region. We ignore the cold filament on the  $z$ -axis because the imposed symmetry of our 2D cylindrical calculations might result in enhanced on-axis cooling. Moreover, we neglect the effect of the relativistic jet, from which the cavity likely originates, that can modify the velocity structure of the gas on the axis.

Figure 9 shows the distribution of the  $z$ -component of the cold gas velocity for several no-dropout models, in the cavity region. Generally, both inflowing and outflowing cold clouds are present, with no clear trend. Cold outflows form from outward moving hot gas and are not clouds dragged from the center by the cavity-induced motion (see also Costa et al. 2014). Most cold gas has  $v_z$  in the range  $[-200, +200] \text{ km s}^{-1}$ , although high velocity outflows with  $v_z \sim 400 \text{ km s}^{-1}$  are sometime present (Figure 9) We do not find an obvious correlation between maximum outflow velocity and the power of the cavity. The model with  $E_{cav} = 1.17 \times 10^{58}$  ergs (Section 3.5) generates cold outflows with velocity comparable to the the model with  $E_{cav} = 1.17 \times 10^{57}$  ergs and cavity at 2

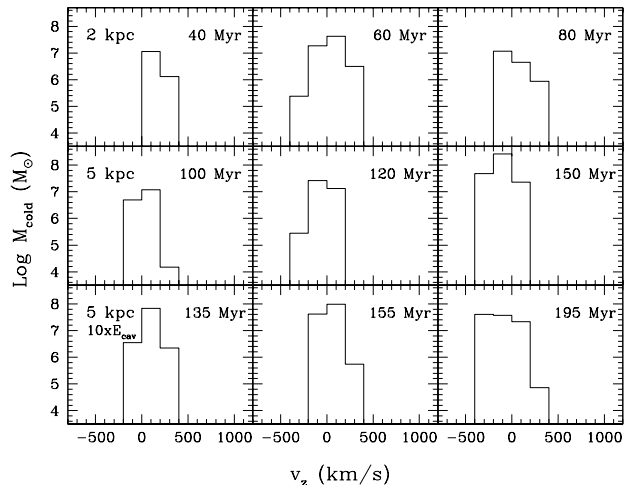


FIG. 9.— Distribution of the cold gas  $z$ -component velocity for three no-dropout models in the cavity region at several times. Positive velocities indicate outflowing gas. In the top row is shown the model with the cavity at  $z = 2$  kpc ( $E_{cav} = 1.17 \times 10^{57}$  ergs). The middle row illustrates the model with the cavity at  $z = 5$  kpc ( $E_{cav} = 1.17 \times 10^{57}$  ergs). The bottom row shows the cavity model with  $E_{cav} = 1.17 \times 10^{58}$  ergs, located at  $z = 5$  kpc.

kpc. At late times the cold gas, which is always bound to the system, tends to fall to the center and the velocity distribution becomes slightly skewed toward negative values.

Recent ALMA observations of massive central galaxies (Russell et al. 2014, McNamara et al. 2014), show molecular gas with velocity up to  $\sim 500$  km s $^{-1}$ . If these velocities are representative of outflowing material, it is likely that multiple cavities or AGN outflows are necessary to explain these properties. Valentini & Brighenti (2015) discuss in more detail the velocities and masses of cooled gas stimulated by many recurrent outflows and cavities in the same hot gas atmosphere.

### 3.7. Ultra-high resolution

To demonstrate computational convergence, some of the solutions shown in Figures 2, 3 and 6 with grid size  $\Delta z = \Delta R = 20$  pc have been repeated at even higher numerical resolution,  $\Delta z = \Delta R = 5$  pc. Figure 10 shows five ultra-high resolution density images of the 2 kpc cavity evolution with and without cooling dropout. At 50 Myrs the first and third panels in Figure 10 closely resemble the lowest two panels in Figure 2 and the density snapshots are similar for all four images at 50 Myrs, dropout or no-dropout. But shortly thereafter at time 60 Myrs, the morphology seen in the ultra-high resolution buoyant 2 kpc cavity becomes sensitive to the dropout assumption. (A similar drastic change occurs during 50-60 Myr at the previous 20 pc grid size.) Between 50 and 60 Myrs the no-dropout 2 kpc cavity shrinks in the  $R$ -direction, possibly due to hot gas cooling onto many small, dense overcooling regions seen across the base of the rising cavity. During this same time interval, the  $R$  dimension of the dropout flow remains unchanged, but the vortical upflow pinches the buoyant 5 kpc cavity in the  $z$ -direction. Soon afterward, the pinched-off part of the cavity will become a torus. This pinching is less pronounced in the no-dropout solution possibly because of the combined inertia of dense cold gas remaining at the bottom of the cavity at  $t = 60$  Myr. We draw attention to

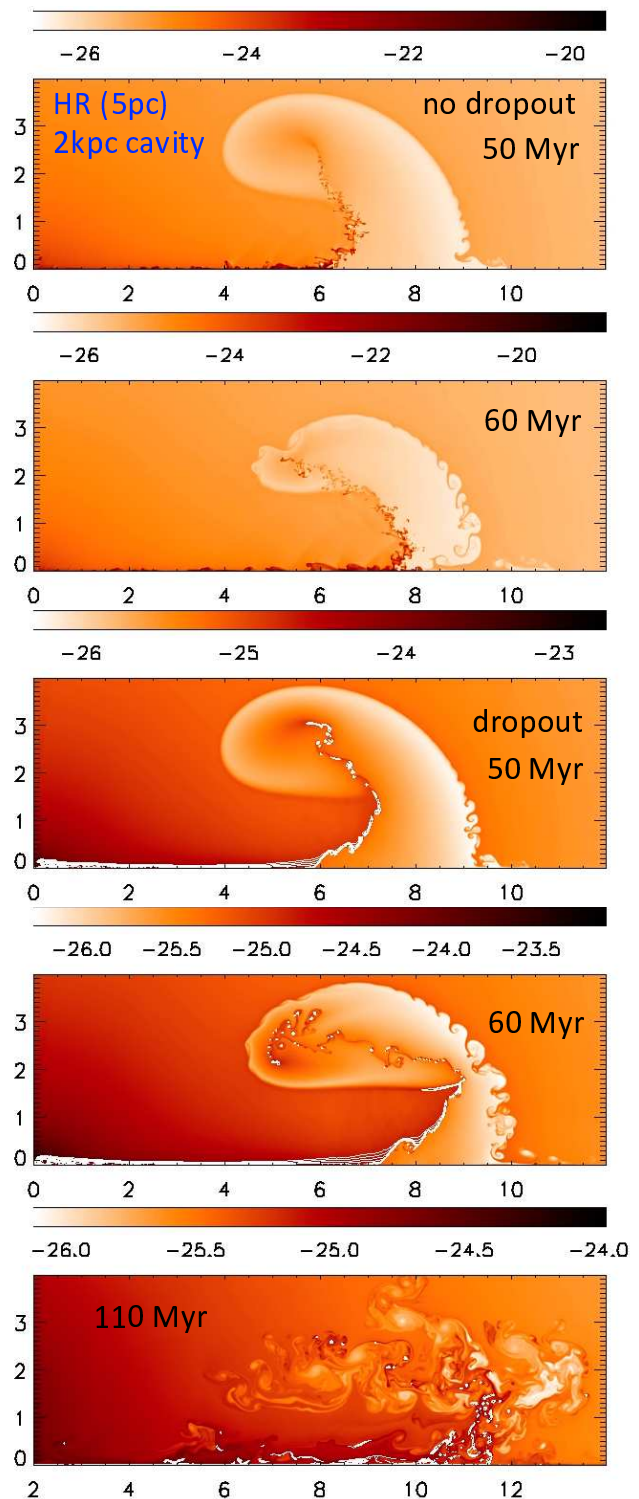


FIG. 10.— Ultra-high resolution ( $\Delta z = \Delta R = 5$  pc) density images of the 2 kpc cavity at 50 and 60 Myrs with and without dropout.

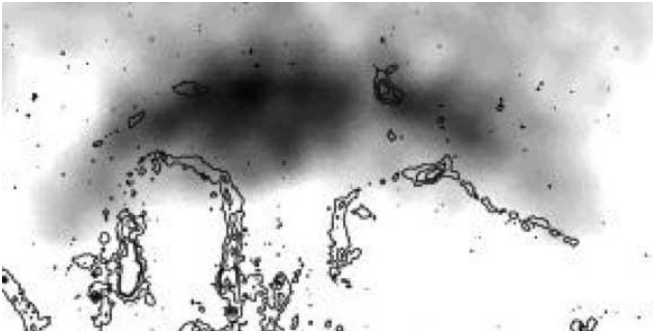


FIG. 11.— The buoyant and flattened northwestern cavity in the Perseus cluster (shown darkened) is rising from the cluster center about 2 cavity diameters vertically below the figure (Fabian et al. 2003). Contours show H $\alpha$  emission below the cavity that resemble the cooling regions computed here.

the Rayleigh-Taylor and Kelvin-Helmholtz features seen in Figure 10 along the front and side of the cavity at time 60 Myr. The lowest dropout panel in Figure 10 shows the disrupted 2 kpc cavity at 110 Myrs. Finally, the green long-short dashed line in Figure 4 shows the no-dropout cooling rate for the 2 kpc cavity at ultra-high 5 pc resolution which faithfully follows the unphysical overcooling peak of the  $\Delta z = \Delta R = 20$  pc solution (solid line). This agreement not only verifies computational convergence, but also shows that the unphysical overcooling in this peak cannot simply be removed with higher computational resolution or by employing adaptive mesh refinement (AMR).

### 3.8. Similar cooling filaments in the Perseus cluster

In support of the early time cavity cooling patterns illustrated in Figures 2, 3 and 7, we show in Figure 11 a remarkably similar H $\alpha$  filament observed in the northwestern cavity in the Perseus cluster (Fabian et al. 2003). The flattened mushroom shape of this cavity indicates that is buoyantly rising in the cluster gas. We propose that these observed filaments are edge-brightened toroidal features that qualitatively resemble the toroidal cooled gas filaments we calculate here. These curved filaments in Perseus do not indicate that the much colder and denser H $\alpha$  emitting gas is “being dragged” outward in the atmosphere by the rising cavity, as many authors have suggested, nor do the Y-shaped filaments represent stream lines as the gas flows underneath the cavity. Instead, when interpreted with our calculations, the curved filaments in Figure 11 define a transient cooling locus where the vortical upwelling of cluster gas presses against the bottom of the rising cavity. However, the lower approximately radial segments of the Perseus filaments remain parallel and open along the symmetry axis pointing toward the cluster center. This feature differs from our computed Y-shaped filaments in which the vertical elements of the filament are coincident along the  $z$ -axis. The separation of the parallel vertical segments of the H $\alpha$  filament observed in Perseus may be due to the influence of the jet that created the cavity which we do not consider.

## 4. SUMMARY AND CONCLUSIONS

Confidence in computations of Eulerian cavity hydrodynamics with radiative losses in group/cluster atmo-

spheres is only possible when several numerical pitfalls are avoided. It is essential to avoid overcooling when small, high density cooled regions move across the computational grid, seeding additional unphysical overcooling which can greatly exceed the mass of the original cooled regions. We show that numerical overcooling can be avoided by invoking subgrid cooling dropout in which gas is removed from the computational grid before it cools below some very low temperature. Spurious overcooling is also limited computations with high numerical resolution, Time steps must be shortened to smoothly follow the decreasing temperature at every cooling site in the flow. The volume occupied by gas that cools to low temperatures is insignificant and its removal does not upset the overall dynamics of the remaining hot gas. The same numerical thermal mixing responsible for overcooling can lead to undercooling in localized regions having only slightly smaller entropy than the ambient gas. In this case the entropy in the perturbation may rise faster by numerical mixing than it decreases by radiative losses, leading to an underestimate of the cooling rate. Numerical undercooling is more difficult to detect and avoid than overcooling, but when radiative cooling occurs in computations with dropout, this provides a physically useful lower limit on the total mass of gas that actually cools.

Detailed high resolution computations of the rise and demise of buoyant cavities demonstrate beyond doubt that cavities visible in X-ray group/cluster atmospheres stimulate inhomogeneous, spatially extended, off-center cooling of significant masses of hot gas. Cooling occurs in an ordered fashion during the early evolution of cavities and later in a more disordered fashion long after the initially spatially coherent cavities have irreversibly fragmented and disrupted. Cavity-induced cooling is expected to be universal in hot gaseous atmospheres in galaxy groups and clusters, but it may not always be observable due to variations in the cooling rate. To illustrate cooling associated with buoyant cavities, we compute cavity hydrodynamics in the well-studied hot atmosphere of the NGC 5044 group which is known to have three spatially extended multi-phase components: optical line emission from warm gas, far infrared dust emission, and submillimeter emission from molecular gas. Apparently, most of the observed low temperature gas currently in NGC 5044 is molecular.

To investigate off-center cooling, we consider the inflation of single axisymmetric cavities in an idealized, perfectly static hot gas atmosphere resembling NGC 5044. The earliest off-center cooling appears beneath the cavity along the symmetry axis. Shortly afterward, cooling appears across the bottom of the buoyant cavity as it flattens along the direction of its buoyant trajectory (i.e. the local radial direction in the group atmosphere). Radiative cooling in both regions is driven by a large vortex of cluster gas flowing around the buoyant cavity that provides a long-lasting compression and differential entropy loss from the hot gas. Our computed cooling in the radial filament and cavity regions combine to create a filamentary Y-shaped cooling pattern in projection that resembles, on a smaller scale, the iconic post-cavity flow observed in the big buoyant northwestern cavity the Perseus cluster.

As expanding X-ray cavities form in the hot atmo-

spheres of galaxy groups and clusters, they drive shocks into the hot gas that provide an important source of feedback heating required to offset radiative losses and catastrophic central cooling. In this paper we show that cavities also stimulate limited radiative cooling in cluster gas that is compressed in the wakes of their buoyant flow. Although the net effect of cavities is to increase the entropy of cluster atmospheres by shock dissipation etc., cavities also lower the entropy in significant and observable masses of gas, some or most of which may cool to form gravitationally unbound molecular regions similar to those observed in the NGC 5044 group (David et al. 2014) and elsewhere (e.g. O’Sullivan et al. 2014).

Localized cooling dropout continues long after the X-ray cavity disrupts and is difficult to observe. Late time inhomogeneous cooling in the cavity region ( $z > 1$  kpc  $R > 0.3$  kpc) can dominate the total mass of gas that ultimately cools near the center. Evidently, the range in times gas spends at various densities during the early vortex compression imprints a range of lowered entropy that cools at various times afterwards. This later cooling occurs in isolated regions or in small non-radial filaments/regions distributed nearly isotropically near the cluster center. More energetic cavities stimulate more off-center cooling. The total mass of off-center (cavity region) cooled (dropped out) gas created by a single cavity of energy  $10^{56} - 10^{57}$  ergs in the galaxy group NGC 5044,  $10^8 - 10^9 M_{\odot}$ , exceeds the total mass of extended molecular gas  $\sim 10^8 M_{\odot}$  recently observed in NGC 5044 with the 30m IRAM and ALMA telescopes.

Our cavity calculations are performed as a cooling flow develops in the cluster atmosphere. The cooling flow is

modified, but not eliminated, by a single cavity which cannot provide enough sustained energy. Cooling flows can be stopped by computing a series of intermittent cavities having various energies and distances from the cluster center (Mathews 2009). When feedback cavity energy balances radiative losses, the time-averaged gas density and temperature profiles in the hot atmosphere are kept roughly constant. When this balance is achieved, the net radial flow of cluster gas approaches zero, but radial gas motions are by no means eliminated. Even when cooling flows are largely arrested, some buoyant outflow of high-entropy gas continues due to recent cavities. Low entropy gas first flows outward in the vortex flow that compresses against the buoyant cavity, then, having radiated away some of its entropy, ultimately sinks back toward the cluster center taking  $\sim 10^8$  yrs. As this low-entropy, slightly denser gas approaches the cluster core, it cools to low temperatures before arriving at the cluster center. Consequently, when a cooling flow is properly arrested with multi-cavity feedback, we may expect warm and/or molecular clouds to form near the central galaxy.

Studies of the evolution of hot gas in elliptical galaxies at UC Santa Cruz were supported during the earlier phases of this work by the NSF and are currently supported by a NASA-funded Chandra Theory Grant for which we are very grateful. FB is supported in part by the Prin MIUR grant 2010LY5N2T “The Chemical and Dynamical Evolution of the Milky Way and Local Group Galaxies”.

## REFERENCES

- Brighenti, F. & Mathews, W. G. 2002, *ApJ* 573, 542  
 Brighenti, F. & Mathews, W. G. 2003, *ApJ* 587, 580  
 Bruggen, M., 2003, *ApJ* 592, 839  
 Bruggen, M., Scannapieco, E., Heinz, S., 2009, *MNRAS* 395, 2210  
 Buote, D., Lewis, A., Brighenti, F., Mathews, W. G. 2003, *ApJ* 594, 741  
 Buote, D., Brighenti, F., Mathews, W. G. 2004, *ApJ* 607, L91  
 Combes, F., Salome, P.  
 Conselice, C. J., Gallagher, J. S., III, & Wyse, R. F. G. 2001, *AJ*, 122, 2281  
 Costa, T., Sijaki, D., Haehnelt, M., 2014, arXiv:1411.0678  
 Dalla Vecchia, C., Bower, R.G., Theuns, T., Balogh, M.L., Mazzotta, P., Frenk, C.S., 2004, *MNRAS* 355, 995  
 David, L. P. et al. 2014, *ApJ* 792, 94  
 David, L. P. et al. 2011, *ApJ* 728, 162  
 David, L. P., Jones, C., Forman, W., Daines, S. 1994, *ApJ* 428, 544  
 David, L. P., Jones, C., Forman, W., Nulsen, P., Vrtilek, J., O’Sullivan, E. 2009, *ApJ*, 705, 624  
 Dennis, T.J., Chandran, B.D.G., 2005, *ApJ* 622, 205  
 Dong, R., Stone, J. M., 2009, *ApJ*, 704, 1309  
 Fabian, A. C.; Johnstone, R. M.; Sanders, J. S.; Conselice, C. J.; Crawford, C. S.; Gallagher, J. S., III; Zweibel, E., 2008, *Nature*, 454, 968  
 Fabian, A. C.; Sanders, J. S.; Crawford, C. S.; Conselice, C. J.; Gallagher, J. S.; Wyse, R. F. G., 2003 *MNRAS* 334, L48  
 Fabian, A. C., Nulsen, P. E. J., & Canizares, C. R. 1984, *Nature* 310, 733  
 Gardini, A., 2007, *A&A* 464, 143  
 Gaspari M., Ruszkowski, M., Sharma, P., 2012, *ApJ*, 746, 94  
 Guo, F., Mathews, W. G. 2011, *ApJ* 728, 121  
 Ho, I.-T., Lim, J., & Dinh-V-Trung 2009, *ApJ*, 698, 1191  
 Koyama, H., Inutsuka, S., 2004, *ApJ*, 602, L25  
 Jones, T. W.; De Young, D. S., 2005, *AJ* 624, 586  
 Lim, J., Ohyama, Y., Yan, C.-H., Y., Dinh-V-Trung, Wang, S.-Y., 2012, *ApJ*, 744, 112  
 Loewenstein, M. 1989, *MNRAS* 238, 15  
 Malagoli, A., Rosner, R., Bodo, G. 1987, *ApJ* 319, 632  
 Mathews, W. G. 2009, *ApJ* 695, L49  
 Mathews, W. G., Temi, P., Brighenti, F., Amblard, A., 2013, *ApJ* 768 23  
 Mathews, W. G. & Guo, F., 2011, *ApJ* 738, 155  
 Mathews, W. G. & Brighenti, F. 2008, *ApJ*, 676, 880  
 Mathews, W. G. & Brighenti, F. 2003, *Ann. Rev. Astron. Ap.* 41, 191  
 McCourt, M., Sharma, P., Quataert, E., Parrish, I.J., 2012, *MNRAS*, 419, 3319  
 McDonald, Michael; Veilleux, Sylvain; Rupke, David S. N., 2012, *ApJ* 746, 153  
 McDonald, M., Veilleux, S., Mushotzky, R. 2011a, *ApJ* 731, 33  
 McDonald, M., 2011b, *ApJ* 742, L35  
 McNamara, B.R., Russell, H.R., Nulsen P.E.J., et al., 2014, *ApJ* 785, 44  
 O’Neill, S. M.; De Young, D. S.; Jones, T. W., 2009, *ApJ* 694, 1317  
 O’Sullivan, E.; Combes, F.; Hamer, S.; Salome, P.; Babul, A.; Raychaudhury, S., 2014, (arXiv1408.7106).  
 Panagoulia, E. K.; Fabian, A. C.; Sanders, J. S.; Hlavacek-Larrondo, J., 2014, (arXiv1407.6614)  
 Revaz, Y., Combes, F., Salome, P. 2008, *A&A* 477, L33  
 Reynolds, C. S., McKernan, B., Fabian, A. C., Stone, J. M., vernaleo, J. C., 2005, *MNRAS* 357, 242  
 Russell, H.R., McNamara, B.R., Edge, A.C., et al. 2014, *ApJ* 784, 78  
 Ruszkowski, M., Ensslin, T. A., Bruggen, M., Heinz, S., Pfrommer, C., 2007, *MNRAS* 378, 662  
 Salome, P., Combes, F., 2004, *A&A* 415, L1  
 Sharma, P., McCourt, M., Quataert, E., Parrish, I.J., 2012, *MNRAS*, 420, 3174  
 Stone, J.L., & Norman M.L. 1992, *ApJS* 80, 753  
 Sutherland, R. S. & Dopita, M. A. 1993, *ApJS* 88, 253  
 Valentini, M., Brighenti, F., 2015, *MNRAS*, in press  
 Werner, N. et al. 2014, *MNRAS* 439, 2291  
 Werner, N. et al. 2013, *ApJ* 767, 153  
 White, R. E. III. & Sarazin, C. L. 1987, *ApJ* 318, 612